Kinetic and Structural Evolution of Self-gravitating, Magnetized Clouds: 2.5-Dimensional Simulations of Decaying Turbulence

Eve C. Ostriker[1], Charles F. Gammie[2,3], and James M. Stone[1]
[1]Department of Astronomy, University of Maryland
College Park, MD 20742-2421
[2]Isaac Newton Institute for Mathematical Sciences
20 Clarkson Rd., Cambridge, CB3 0EH, UK
[3]Harvard-Smithsonian Center for Astrophysics, MS-51
60 Garden St., Cambridge, MA 02138

ABSTRACT

The molecular component of the Galaxy is comprised of turbulent, magnetized clouds, most of which are self-gravitating and form stars. To model how these clouds' kinetic and structural evolution may depend on their level of turbulence, mean magnetization, and degree of self-gravity, we perform a survey of direct numerical MHD simulations in which three parameters are independently varied. Our simulations consist of solutions to the time-dependent MHD equations on a two-dimensional grid with periodic boundary conditions; an additional "half" dimension is also incorporated as dependent variables in the third Cartesian direction. Two of our survey parameters – the mean magnetization parameter $\beta \equiv c_{sound}^2/v_{Alfven}^2$ and the Jeans number $n_J \equiv L_{cloud}/L_{Jeans}$ – allow us to model clouds which either meet or fail conditions for magneto-Jeans stability and magnetic criticality. Our third survey parameter – the sonic Mach number $\mathcal{M} \equiv \sigma_{velocity}/c_{sound}$ – allows us to initiate turbulence of either sub- or super- Alfvénic amplitude. We evaluate the times for each cloud model to become gravitationally bound, and measure each model's kinetic energy loss over the fluid flow crossing time. We compare the evolution of density and magnetic field structural morphology, and quantify the differences in the density contrast generated by internal stresses, for models of differing mean magnetization. We find that the values of β and n_J, but not the initial Mach number $\mathcal{M}$, determine the time for cloud gravitational binding and collapse: unmagnetized models collapse after $\sim$ 5Myr, magnetically supercritical models generally collapse after $5-10$Myr (although the smallest magneto-Jeans stable clouds survive gravitational collapse until $t \sim$ 15Myr), while magnetically subcritical clouds remain uncollapsed over the entire simulations. We find, contrary to some previous expectations, less than a factor of two difference

between turbulent decay times for models with varying magnetic field strength; the maximum decay time, for $B \sim 14\mu$G, is $\sim$ 10Myr. In all models, we find turbulent amplification in the magnetic field strength up to at least the level $\beta_{pert} \equiv c^2_{sound}/\delta v^2_{Alfven} = 0.1$. We find that for weakly self-gravitating stages of evolution, when clouds have $\mathcal{M} = 5 - 10$, the mass-averaged density contrast magnitudes $\langle \log(\rho/\bar{\rho}) \rangle$ are in the range $0.2 - 0.5$, with the contrast increasing both toward low- and high- β; only the more strongly-magnetized models appear consistent with clump/interclump density contrasts observed in Galactic GMCs.

1. Introduction

All present-day star formation in our Galaxy is observed to take place in cold molecular clouds. These clouds are highly turbulent (with sonic Mach numbers 10 or more for the most massive clouds, e.g. Blitz (1993)), and appear to be quite inhomogeneous based on both molecular line observations in a range of tracers (e.g. Falgarone, Puget, & Pérault (1992), Falgarone et al (1998)), and stellar extinction maps (Lada et al (1994), Lada, Alves, & Lada (1998)). Because magnetic field measurements are difficult to obtain, the distributions of magnetic field strengths and directions within clouds are less well characterized than other cloud properties; the mean field strengths are probably no less than a few μG, and no more than a few tens of μG (e.g. Heiles et al. (1993), Crutcher et al (1993), Troland et al (1996), Crutcher (1998)), and the spatial power spectrum of the magnetic field is probably dominated by components with close to the largest scales possible, within a structures of a given density regime (e.g. Goodman & Heiles (1994), Goodman et al (1995), Schleuning (1998)) Given the extremely low thermal pressure in molecular clouds, magnetic stresses are expected to be at least as important as gas pressure in governing cloud evolution, and may be much more so. In particular, since sufficiently strong mean magnetic fields would render the internal motions sub-Alfvénic and the cloud self-gravity subcritical, it has long been argued that magnetization may significantly inhibit turbulent dissipation and prevent gravitational collapse (Arons & Max (1975), Mouschovias & Spitzer (1976), Shu et al. (1987), McKee et al. (1993)).

The nonlinear amplitudes and structural irregularity of the turbulence seen in molecular clouds require time-dependent numerical simulations in order to model their evolution theoretically. This is the second in a series of papers reporting on the results of numerical experiments designed to characterize how magnetic fields at a range of strengths affect the structure and evolution of cold, turbulent, self-gravitating clouds. In Paper I (Gammie & Ostriker (1996)), we outlined (see also Ostriker (1997)) the observational situation, the

theoretical background on the nature of ideal turbulent flows and applications to cold Galactic clouds, and the issues that can be addressed by numerical simulations; we then presented results of the first extensive survey (in "1 2/3D" slab geometry, i.e. with one independent spatial variable, but all three components of dependent spatial variables) of model cloud evolution in the ideal MHD limit. The survey considered clouds both with and without gravity, and either with an input spectrum of turbulence that decayed over time, or with an ongoing excitation of turbulence through velocity perturbations introduced at spatial scales smaller than the simulation box. Among the conclusions of Paper I was the finding that, when sufficient initial energy in the form of transverse disturbances is input to a cloud model and then evolved, gravitational collapse along the mean field can be suppressed for times $> t_g$ (see eq. 3 below). Paper I also reported on the large density contrasts, and correspondingly small filling factors, which arise in freely-decaying turbulent MHD flows (e.g. a typical model having 50% of the mass at density larger than three times the mean, and 10% of the mass at nine times greater than the mean). Because these conclusions could potentially be affected by the restricted geometry of the slab-symmetric models – where no spatial variations perpendicular to the mean field are possible – we re-examine these issues in the present paper with a less restricted geometry.

Recent numerical work by other groups has addressed a variety of related questions. Elmegreen (1997) has found that hierarchical density structure arises in 1D MHD cloud models which are subject to mechanical forcing at their boundaries. Passot, Vazquez-Semadeni, & Pouquet (1995) and Vazquez-Semadeni, Passot, & Pouquet (1996) have modeled cloud formation and evolution in the ISM on $\sim$ kpc scales, incorporating a number of physical effects (Galactic rotation and shear, heating from localized star formation, and cooling) in addition to magnetic fields. Padoan & Nordlund (1997) and MacLow et al (1998) have simulated the decay of Mach-5 turbulence in 3D cloud models with weak ($c_s^2/v_A^2 = 2, 1$, respectively) and moderate ($c_s^2/v_A^2 = 0.02, 0.04$, respectively) magnetic fields, and find less than a factor 2 difference in the kinetic energy decay for the two cases.

Because the matter distributions in clouds should eventually influence star formation and the IMF, numerical modelers have taken a particular interest in analyzing the density structure of their simulated clouds. In particular, there has been considerable recent attention devoted to the shape of the density distribution function obtained in simulations of compressible turbulence. Based on a variety of non-self-gravitating simulations at varied Mach numbers, with/without turbulent forcing, and using a variety polytropic indices γ, two different groups (Padoan, Jones, & Nordlund (1997), Nordlund & Padoan (1998); Scalo et al (1998), and Passot & Vazquez-Semadeni (1998)) have concurred in finding that log-normal density distributions are expected when $\gamma = 1$, and skewed log-normal/power law distributions are expected when $\gamma \neq 1$. These groups differ, however, in their predictions

of the scaling of the mean density contrast magnitude with Mach number.

In this paper, we extend our previous slab-geometry survey (Paper I) by performing a survey in 2 1/2 dimensions[1] of the evolution of turbulence in model clouds with a range of sizes, Mach numbers, and magnetizations. §2 describes our numerical experiments, including the computational code we use (§2.1), the definitions of relevant dimensionless parameters (§2.2), and our choices of parameters for the survey (§2.3). In §3, we present our results on the evolution of cloud energies (§3.1), structural appearance (§3.2), and density distributions (§3.3) in our models. We summarize our results and discuss the principal implications of our work for the evolution and structure of observed clouds in §4.

2. Simulations

2.1. Numerical Method

To create the model cloud evolutions presented in this paper, we integrate the equations of ideal, compressible, self-gravitating MHD using a variant of the ZEUS algorithm developed by Stone & Norman (1992a), Stone & Norman (1992b). ZEUS is an operator-split, finite difference method on a staggered mesh. The magnetic field is evolved using "constrained transport" (Evans & Hawley (1988)), which guarantees that $\nabla \cdot \mathbf{B} = 0$ to machine precision. The transverse components of the magnetic field are evolved using the "method of characteristics" which guarantees accurate propagation of Alfvénic disturbances. Dissipation occurs on small scales in part due to purely numerical effects associated with discretizing the MHD equations (i.e. from zone-to-zone averaging of velocity, magnetic field, or density variations), and in part due to an artificial viscosity introduced to capture shocks. The algorithm has been extensively tested and used in a wide variety of astrophysical applications.

Our implementation of ZEUS is "2 1/2 dimensional" (2.5 D). This peculiar nomenclature means that there are two independent spatial variables (x, y), but that all (three) components of the velocity and magnetic field vectors are still evolved as dependent variables. In this sense, there are two fully dynamical dimensions and a third dimension in which the flow is symmetric. The boundary conditions in all models are periodic.

The gravitational potential is determined from $\nabla^2\phi = 4\pi G(\rho - \bar{\rho})$; the mean density

[1]I.E. two spatial independent variable, but three spatial components to all dependent variables; this allows spatial variations both parallel and perpendicular to the mean magnetic field.

appears because of the periodic boundary conditions. We solve for the gravitational potential using the Fourier method. The gravitational kernel is

$$\phi_{\mathbf{k}} = 2\pi G\rho_{\mathbf{k}} \left((1-\cos(k_x\Delta x))/\Delta x^2 + (1-\cos(k_y\Delta y))/\Delta y^2\right)^{-1}. \quad (1)$$

This ensures that the discrete representation of Poisson's equation is satisfied.

We adopt, for all models, an isothermal equation of state, meaning that $p = c_s^2\rho$, where c_s^2 is a constant in both space and time. Thus we do not integrate an internal energy equation. This is a physically reasonable approximation for molecular clouds because the cooling time is very short (e.g. Goldsmith (1987) and references therein).

For all the simulations, we choose the initial velocity field to be locally divergence-free (i.e. the individual Fourier components are constrained to satisfy $\mathbf{v_k}\cdot\mathbf{k} = 0$), and isotropic in direction. The velocity amplitude is drawn from a Gaussian distribution with power spectrum $\langle|\mathbf{v_k}|^2\rangle \propto k^{-3}$, for $k = |k_x\hat{x} + k_y\hat{y}|$ and $2\pi/L \leq k_i \leq 128(2\pi/L)$. The initial kinetic energy therefore obeys $E = \Sigma_{k_x,k_y}E_{\mathbf{k}}$ where $E_{\mathbf{k}} = (1/2)v_{\mathbf{k}}^2 \propto k^{-3}$, corresponding to a relationship $\sigma_v(R) \propto R^{1/2}$ between size scale R and the velocity dispersion σ_v averaged over that scale.

Initially, the density for all models is taken to be uniform; all inhomogeneities are generated self-consistently from divergences in the velocity field created by internal pressure forces, gravity, and magnetic stresses (since $\nabla\cdot\mathbf{v} = 0$ initially). The initial magnetic field is also taken to be uniform, pointing in the $\hat{x}$ direction (right-left in the model snapshots shown). Notice that the uniformity of $\mathbf{B}$ and ρ in the initial conditions implies that the mass-to-flux ratio along each field line is constant. In snapshots shown, the symmetric direction $\hat{z}$ points out of page.

We have tested our implementation of the ZEUS algorithm using a variety of test problems: linear waves, standard advection tests, shock tubes and the parametric instability of circular polarized Alfvén waves. Of particular interest for what follows is whether the simulations are converged at our standard resolution, 256^2 zones. We have tested this by evolving an initial Gaussian random velocity field, as in all our decay experiments, while holding the amplitude and phase of the field's Fourier components fixed as the resolution is increased from 32^2 to 512^2 zones. The convergence test models use $n_J = 2.5$, $E_{K,init} = 50$, and $\beta = 0.02$ (see §2.2 for definitions). We find a secular decrease in the ratios E^{2n}/E^n of turbulent energies ($\equiv$ perturbed magnetic and kinetic energy) at successive resolutions; at time $0.1t_s$ these ratios decrease from $E^{64}/E^{32} = 1.19$ to $E^{128}/E^{64} = 1.11$ to $E^{256}/E^{128} = 1.08$ to $E^{512}/E^{256} = 1.06$. We also find only a 5% difference in the gravitational binding time (see §3.1) between the 256^2 and 512^2 models. Thus, at a resolution of 256^2 zones, the evolution is satisfactorily converged.

2.2. Scalings and definitions

The fundamental dimensional units for our simulations are the length L of the box edge, the mean density $\bar{\rho} = M/L^3$ of matter in the box, and the (isothermal) sound speed $c_s = \sqrt{kT/\mu}$. Because self-gravity is crucial in the problems under study, it is useful to describe the size of the simulated region relative to the minimum Jeans-unstable wavelength $L_J \equiv c_s(\pi/G\bar{\rho})^{1/2}$ at the cloud's mean density and temperature. For each simulation we therefore define the size via the Jeans number $n_J \equiv L/L_J$; using $c_s = 0.19\,\mathrm{km\,s^{-1}}(T/10\mathrm{K})^{1/2}$ for $\mu = 2.4m_p$ the corresponding physical size is

$$L = n_J L_J = n_J \times 1.9\,\mathrm{pc}\left(\frac{T}{10\mathrm{K}}\right)^{1/2}\left(\frac{n_{H_2}}{10^2\mathrm{cm}^{-3}}\right)^{-1/2}. \tag{2}$$

With the parameter values $n_J = 2, 3, 4$ used in the present simulations, the box edge would respectively correspond to approximately $4, 6,$ or 8pc at the mean conditions in a molecular cloud ($n_{H_2} \sim 100$), a factor 3 smaller for conditions within a cloud clump ($n_{H_2} \sim 10^3$), or a factor 10 smaller for conditions in a dense core ($n_{H_2} \sim 10^4$).

Time in our numerical experiments is measured either in units of the sound-crossing time $t_s = L/c_s$ for the simulated region, or in terms of a characteristic gravitational contraction time $t_g \equiv L_J/c_s = (\pi/G\bar{\rho})^{1/2}$.[2] The corresponding physical time depends on the mean density according to

$$t_g = t_s/n_J = 9.9\,\mathrm{Myr}\left(\frac{n_{H_2}}{10^2\mathrm{cm}^{-3}}\right)^{-1/2}. \tag{3}$$

Thus for $n_J = 2, 3,$ or 4, the interval $0.1t_s$ would respectively correspond to approximately $2, 3,$ or 4 Myr at the typical mean density in a molecular cloud, and a factor 3 or 10 shorter at clump or core densities; the interval $0.1t_g \sim 1$Myr at typical mean GMC conditions.

The total mass within a cube with faces the same size as the simulated region corresponds to $M = n_J^3 M_J$, where the Jeans mass at the mean conditions is

$$M_J \equiv \bar{\rho}L_J^3 = 48\ \mathrm{M}_\odot\left(\frac{n_{H_2}}{10^2\mathrm{cm}^{-3}}\right)^{-1/2}\left(\frac{T}{10\mathrm{K}}\right)^{3/2}. \tag{4}$$

At the beginning of all the simulations, the magnetic field is uniform with strength B_0 and points in the $\hat{x}$ direction. The level of the mean magnetic field in each simulation is

[2]For reference, the free-fall collapse times for a cold sheet, cylinder, or sphere are, respectively $0.25t_g$, $0.28t_g$, and $0.31t_g$.

characterized by the ratio

$$\beta \equiv \frac{c_s^2}{v_A^2} = \frac{c_s^2}{B_0^2/(4\pi\bar{\rho})} = 0.021 \left(\frac{T}{10\mathrm{K}}\right) \left(\frac{n_{H_2}}{10^2\mathrm{cm}^{-3}}\right) \left(\frac{B_0}{10\mu\mathrm{G}}\right)^{-2} \tag{5}$$

corresponding to $B_0 = 1.4\mu\mathrm{G}\beta^{-1/2} \left(\frac{T}{10\mathrm{K}}\right)^{1/2} \left(\frac{n_{H_2}}{10^2\mathrm{cm}^{-3}}\right)^{1/2}$; decreasing β corresponds to increasing the importance of magnetic fields to the dynamics. For the values $\beta = 0.01,\ 0.1, 1.0$ used in the present set of simulations, the mean magnetic field is $B_0 = 14,\ 4.4$, and 1.4μG respectively, for fiducial values $T = 10$K and $n_{H_2} = 100\mathrm{cm}^{-3}$.

Uniform clouds are unstable to compressions transverse to the mean magnetic field ("magneto-Jeans unstable") when the magnetosonic wave crossing time exceeds t_g (Chandrasekhar & Fermi (1953)); for $v_A >> c_s$ this occurs when $n_J > \beta^{-1/2}$, corresponding to having the cross-field column density $N_{H_2} > 4.1 \times 10^{21}\mathrm{cm}^{-2}(B_0/10\mu\mathrm{G})$. A closely-related criterion is used to evaluate a more stringent stability condition, as follows: If a uniform cubic cloud with size $L = n_J L_J$ condenses along the mean field to make a cold "pancake," the pancake will have ratio of surface density to magnetic field $\Sigma/B_0 = (n_J\beta^{1/2})/(2G^{1/2})$. This magnetized pancake is unstable to fragmentation when $\Sigma/B_0 > 1/(2\pi G^{1/2})$ [3] (corresponding to $N_{H_2} > 1.3 \times 10^{21}\mathrm{cm}^{-2}(B_0/10\mu\mathrm{G})$), so that the corresponding instability criterion in terms of the original cloud's parameters is $n_J > \beta^{-1/2}\pi^{-1}$. Clouds with $n_J > \beta^{-1/2}\pi^{-1}$ are termed "supercritical;" clouds with the inequality reversed are termed "subcritical."

In terms of the fundamental units, all energies in the problem are given in units of $\bar{\rho}c_s^2L^2$; because the $\hat{z}$ direction is symmetric, this is the energy per unit length dz. For a cubic cloud, the corresponding total energy unit would be $\bar{\rho}c_s^2L^3$. Where the kinetic energy is given, it corresponds to

$$E_K = \frac{1}{2}\int_{-L/2}^{L/2}\int_{-L/2}^{L/2} dxdy(v_x^2 + v_y^2 + v_z^2)\rho; \tag{6}$$

the square of the Mach number $\mathcal{M} \equiv \sigma_v/c_s$ (where σ_v represents the total velocity dispersion) is therefore $\mathcal{M}^2 = (\sigma_v/c_s)^2 = 2[E_K/(\bar{\rho}L^2c_s^2)]$, i.e. twice the normalized kinetic energy. The total magnetic energy corresponds to

$$E_B = \frac{1}{8\pi}\int_{-L/2}^{L/2}\int_{-L/2}^{L/2} dxdy(B_x^2 + B_y^2 + B_z^2); \tag{7}$$

[3]The same instability criterion applies when considering either the ratio Σ/B_0 for a uniform magnetized sheet or the central mass-to-magnetic-flux ratio of a magnetized cloud (Tomisaka, Ikeuchi, & Nakamura (1988)).

for the energy in the perturbed magnetic field, δE_B, we subtract out the mean-field energy $1/(2\beta)$ from equation (7). Because we assume periodic boundary conditions, the mean magnetic field (corresponding to the $k = 0$ Fourier component of $\mathbf{B}$), and hence the mean-field energy, remains unchanged over the course of any simulation. The gravitational energy is

$$E_G = \frac{1}{2}\int_{-L/2}^{L/2}\int_{-L/2}^{L/2} dxdy(\phi\rho) \tag{8}$$

where the gravitational potential is computed from the modified Poisson equation in periodic boundary conditions (§1.1). We note that because equation (1) implies $\phi/c_s^2 \propto L^2 G\bar{\rho}/c_s^2$, the scaled gravitational energy will obey $E_G/(\bar{\rho}L^2c_s^2) \propto n_J^2$.

2.3. Survey Model Parameters

As described in §1, observed clouds present a range of properties, with some more tightly constrained than others. From a theoretical point of view, the observed bulk cloud properties of size, mean magnetization, and velocity dispersion can be described in terms of the dimensionless parameters n_J, β, and $\mathcal{M}^2 = 2[E_K/(\bar{\rho}L^2c_s^2)]$ introduced in §2.2. The well-known correlations between cloud properties (Larson (1981)) can be converted into relationships between these parameters, too. For example, linewidth/size and density/size scalings of the form $\sigma_v \propto L^{1/2}$ and $\bar{\rho} \propto L^{-1/2}$ reported either for whole GMCs (Solomon et al (1987)) or for clumps within GMC's (Bally et al (1987)) can be combined to show that cloud kinetic energy ($E_K \propto \mathcal{M}^2$) and gravitational energy ($E_G \propto n_J^2$) scale together; in terms of the Mach number $\mathcal{M}$ and Jeans number n_J, the observed relationship can be expressed quantitatively as $\mathcal{M} = \sigma_v/c_s = 1.7n_J$. With this observed scaling for sonic Mach number, the corresponding Alfvén Mach number would satisfy $\mathcal{M}_A \equiv \sigma_v/v_A = 1.7n_J\beta^{1/2}$. As a consequence, these observed clouds would be magneto-Jeans unstable ($n_J\beta^{1/2} > 1$) when $\mathcal{M}_A > 1.7$, and magnetically supercritical ($n_J\beta^{1/2} > 1/\pi$) when $\mathcal{M}_A > 0.54$. We can also define a fluid flow crossing time $t_{cross} \equiv L/\sigma_v$; using the observed scalings, this implies $t_g = 1.7t_{cross}$.

In modeling the evolution of decaying turbulence in magnetized, self-gravitating clouds, our survey of numerical experiments brackets the range of observed properties wherever possible. The survey covers a variety of different initial conditions by varying three parameters independently: we set the size of the box to $n_J = 2, 3$, or 4 Jeans lengths (see eq.2), we set the ratio $c_s^2/v_A^2 \equiv \beta = 0.01, 0.1, 1$, or 10^6 (see eq. 5), and we set the initial kinetic energy to $E_{K,init}/(\bar{\rho}c_s^2L^2) = 25, 50$, or 100, corresponding to initial sonic Mach numbers of $\mathcal{M} = 7.1, 10$, or 14. To allow for the decay of turbulent energy, we have set the range of initial kinetic energies slightly higher than estimates of

observed cloud kinetic energies in our range of n_J. The initial Alfvén Mach number $\mathcal{M}_A \equiv \langle v^2/v_A^2 \rangle^{1/2} = (2\beta E_K)^{1/2} = \mathcal{M}\beta^{1/2}$ is 7.1, 10, or 14 for the $\beta = 1$ models; 2.2, 3.2, or 4.5 for the $\beta = 0.1$ models; and 0.71, 1, or 1.4 for the $\beta = 0.01$ models. Thus, all of the models with $\beta = 10^6, 1, 0.1$ have initially significantly super-Alfvénic flow, while the models with $\beta = 0.01$ have initially sub-Alfvénic or slightly super-Alfvénic flow. For $\beta = 1$, all of the model clouds would be unstable by the magneto-Jeans criterion (if initially unperturbed), and also supercritical. For $\beta = 0.1$, the $n_J = 4$ models would be magneto-Jeans unstable and supercritical, while the $n_J = 3, 2$ models would be magneto-Jeans stable but supercritical. For $\beta = 0.01$, the $n_J = 4$ models would be magneto-Jeans stable but supercritical, while the $n_J = 3, 2$ models would be magneto-Jeans stable and subcritical. The set of parameters used for the simulation suite is given in the left three columns of Table 1.

3. Results

3.1. Overall Cloud Energetics

Figure 1 shows the evolution of the total "perturbed" energy $E_{tot} \equiv E_K + \delta E_B + E_G$ for all of the cloud models over the course of the simulations. From Figure 1, it is clear that low-magnetization cloud models become gravitationally-bound – defined as reaching $E_{tot} < 0$ – at significantly earlier times t_{bind} than high-magnetization models, and that the models with the same values of β and n_J (i.e. same mean magnetic field and size) which become bound all do so at close to the same time, regardless of the initial level of turbulent kinetic energy. In Table 1, we list the time t_{bind} (or lower limit) at which the model clouds become bound. The nearly-unmagnetized ($\beta = 10^6$) cloud models all become bound at approximately the same time, $0.5t_g$, regardless of the initial level of kinetic energy or cloud size (i.e. n_J). This is only slightly larger than the time ($\approx 0.3t_g$) that a cold, initially-quiescent cloud would take to collapse; thus, turbulent energy does not in itself do much toward preventing cloud collapse. The $\beta = 1$ models become bound at times between $0.5 - 1.1t_g$, with the larger ($n_J = 4$) clouds collapsing before the smaller ($n_J = 2$) ones. Thus, weakly-magnetized model clouds which have Alfvén Mach numbers larger than one, and are magneto-Jeans unstable, collapse within a factor of two of the time for collapse of completely unmagnetized clouds. The $\beta = 0.1$ model clouds all have initial Alfvén Mach numbers > 1, as well, and are all supercritical. Of these, the $n_J = 4$ models, which are magneto-Jeans unstable, collapse at approximately the same time ($\sim 0.6t_g$) as the nearly-unmagnetized ($\beta = 10^6$) and weakly-magnetized $\beta = 1$ models; the $n_J = 3$ models (which are just barely magneto-Jeans stable) remain unbound until $0.7 - 1.0t_g$, while the magneto-Jeans stable (but supercritical) $n_J = 2$ models evolve to $1.5t_g$ before undergoing

rapid gravitational collapse. For $\beta = 0.01$, all cloud models with $n_{\rm J} = 2, 3$ (which are subcritical) remain unbound up to times at least t_g, with the models with higher initial E_K lasting until the simulations were halted at $1.5t_g$; the supercritical $n_{\rm J} = 4$ clouds lose energy more quickly and collapse at $\sim 0.8t_g$.

Consistent with expectations, the gravitational energy of the subcritical cloud models ($\beta = 0.01$ and $n_{\rm J} = 2, 3$) never exceed the energy of a self-gravitating thin sheet $E_{G,sheet} \approx -[(n_{\rm J}^2\pi^2/6) - 1]$, over the course of the simulations ($t > t_g$; see Table 1). Since the time for an initially-quiescent, cold cloud to collapse to a sheet is just $0.25t_g$, it is clear that the time-dependent magnetic field perturbations have delayed the collapse along the mean field, in subcritical clouds. For the other models that do become bound, the gravitational energy exceeds the energy of a self-gravitating sheet at approximately the same times ($t_{condense}$) as the times when they become bound (t_{bind}) (see Table 1).

For all models, Figure 1 shows that there is an initial phase of rapid kinetic energy loss, with the dissipation rate higher in the models with the larger initial kinetic energy and weaker mean magnetic fields. The time dependence of the kinetic energy dissipation is isolated in Figure 2, which shows the evolution of E_K for all of the cloud models on a log-log scale. Over the period before the matter becomes strongly self-gravitating, the kinetic energy declines approximately proportional to $t^{-0.3}$ in the $\beta = 0.01,\ 0.1$ models, and proportional to $t^{-0.6}$ in the $\beta = 1$ models. The kinetic energy evolution in the $\beta = 10^6$ models does not have a significant period of power-law decay.[4]

Since the simulations described in this paper all describe models of decaying, rather than quasi-steady-state, turbulence, there is no single number which can be used to characterise the turbulent decay rate for each model. However, a useful way to quantitatively characterize the differences in the evolution of the kinetic energy for model clouds of different mean magnetization and size is to compare the total kinetic energy after one crossing time with the initial kinetic energy. We define a characteristic crossing time for the flow as $t_{cross} = L/(2E_{K,\ init})^{1/2}$; for $E_{K,\ init} = 25,\ 50,\ 100$, $t_{cross}/t_s = 0.1414,\ 0.1,\ 0.0707$, respectively. In Table 1, we list the values of the ratio $E_K(t_{cross})/E_{K,\ init}$ for each model cloud. For the $\beta = 0.01$ models, this ratio is in the

[4]In recent work by ourselves (see Stone (1998)) and another group (MacLow et al (1998)), numerical simulations of decaying magnetized and unmagnetized turbulence in 3D have shown that the kinetic energy decline is a steeper function of t. We believe that the difference with the present 2.5D simulations arises because motions in the symmetry direction ($\hat{z}$) are dissipated less easily. Because of the difference between 2.5D and 3D, we regard the present dissipation rates as lower limits; however, we note that the quantitative differences in the magnitude of dissipation between 2.5D and 3D simulations performed to date are not large (see §4.1)

range $0.42 - 0.48$, with the value depending more on the initial kinetic energy than on $n_{\rm J}$ because self-gravity does not become important for any of these model clouds within t_{cross}. For the $\beta = 0.1$ models, all of the models which do not become strongly self-gravitating within t_{cross} have $E_K(t_{cross})/E_{K,\ init}$ smaller than the corresponding values for the $\beta = 0.01$ models; the range is $E_K(t_{cross})/E_{K,\ init} = 0.32 - 0.46$. All of the $\beta = 10^6$ models have smaller values of $E_K(t_{cross})/E_{K,\ init}$ (in the range $0.26 - 0.32$ for uncollapsed models) than the corresponding models with $\beta = 1$, and most of the $\beta = 1$ models have smaller values for this ratio $(0.33 - 0.39)$ than the $\beta = 0.1$ models. Although the trends in the relative levels of dissipation are as expected, with the lower-β cloud models experiencing less dissipation than the higher-β models, there is less than a factor two enhancement of kinetic energy at times t_{cross} in the former compared to the latter. Thus, magnetic fields do reduce dissipation, but when the Alfvén Mach number is of order 0.5 or larger, as for the present set of models (and as expected from estimates of field strengths in self-gravitating molecular clouds), the reduction in dissipation is not large.

In Figure 3, we show the evolution of the perturbed magnetic energy δE_B for all models. Comparison with Figure 2 shows that the perturbed magnetic energy in the $\beta = 0.01, 0.1,$ and 1 models typically increases until it is about a factor 1.5-3 lower than the kinetic energy, and then both decline together. The time to reach the peak magnetic energy increases with increasing β and decreasing $E_{K,\ init}$, and lies in the range $0.1 - 0.25 t_A$ where the Alfvén crossing time $t_A \equiv L/v_{\rm A} = t_s \beta^{1/2}$. Overall, the peak values of δE_B decrease with increasing β, and depend only weakly on $n_{\rm J}$ for any value of $E_{K,\ init}$. A fit to the peak value of δE_B good to $\pm 30\%$ is

$$\delta E_{B,\ max} = 0.3 E_{K,\ init}^{0.8} \beta^{-0.18}; \tag{9}$$

this fit includes only those models with $\beta = 0.01, 0.1, 1$ for which δE_B reaches a maximum and then declines. In Table 2, we list the ratio $\delta E_B / E_K$ after one crossing time. For $\beta = 0.01, 0.1,$ and 1, this ratio varies between 0.25-0.62; for $\beta = 10^{-6}$ this ratio is just $4 - 10 \times 10^{-6}$. Because the peak value of δE_B, the time at which the peak is attained, and the rate of kinetic energy dissipation all depend on β, the ratio $\delta E_B / E_K(t_{cross})$ varies with β for fixed $E_{K,\ init}$; the variation with $n_{\rm J}$ at fixed β and $E_{K,\ init}$ is more moderate. Defining $\beta_{pert} \equiv c_{\rm s}^2 / \delta v_{\rm A}^2 = 1/(2\delta E_B)$, we note that for all the models with $\beta = 0.01$, 0.1, and 1, the minimum value of β_{pert} is 0.1 or smaller; thus, there is dynamical growth of the perturbed magnetic field due to turbulence even when the initial mean field is relatively weak. The amount of growth of the perturbed magnetic field likely depends on the degree of helicity in the initial velocity field (cf. Menneguzzi, Frisch, & Pouquet (1981), Hawley, Gammie, & Balbus (1996)), which is maximal for our choice of a divergence-free initial velocity field.

3.2. Evolution of Cloud Structure

To illustrate the growth of density structure in model clouds, Figure 4 shows density snapshots for the model with $\beta = 0.01$, $n_J = 3$, and $E_{K,\ init} = 50$ at time intervals $0.1t_g$ ($\sim$ 1Myr). This model is magneto-Jeans stable, and marginally subcritical. The early structure, consisting of many small clumps and interconnected filaments, is characteristic of the early appearance of all the models. Over time, the small structures agglomerate into larger structures as kinetic energy is lost to dissipation and gravity does its work. This general process occurs in the other models, as well. However, the late-time structural evolution of the models differs qualitatively depending on the values of β and n_J. In subcritical models, over time gravity causes matter to slide along the magnetic fields and collect into larger filaments (actually the projections of sheets in this 2D geometry) which lie preferentially perpendicular to the mean field. Figure 4 shows how these sheets may continue to oscillate in time. In supercritical models, on the other hand, the self-gravity of the condensations that form is sufficient to overwhelm magnetic stresses, leading to the growth of rounder clumps and eventual gravitational collapse.

Figure 5 compares the development of structure in three cloud models which differ only in the magnitude of their mean magnetic field – having $\beta = 0.01, 0.1$, and 1. The $\beta = 0.01$ model is magneto-Jeans stable and (marginally) subcritical; the $\beta = 0.1$ model is magneto-Jeans stable but supercritical; the $\beta = 1$ model is magneto-Jeans unstable and supercritical. The model clouds all have the same size $n_J = 3$, and all have the same value of $E_{K,\ init} = 50$ (and, in fact, identical initial spatial velocity perturbations). In the $\beta = 0.01$ model, the magnetic field lines remain close to their original, parallel configuration; early-time large oscillations of the matter clumps and filaments bend and compress the field locally. At the final time shown ($t = 0.8t_g$), the matter density remains less than $\rho/\bar{\rho} = 100$ everywhere. In the $\beta = 0.1$ model, the magnetic field is less rigid and hence there are much larger initial departures from parallel lines. Local regions with density $\log(\rho/\bar{\rho}) > 2$ appear in the $t/t_g = 0.5$ snapshot (these contain 3.6% of the total mass), and grow in volume and mass so that at $t/t_g = 0.8$, 18% of the mass is at $\log(\rho/\bar{\rho}) > 2$. The magnetic field becomes more uniform as kinetic energy is lost, but there remain large departures from straight lines in the high-density regions. In the $\beta = 1$ simulation, the magnetic fields immediately become strongly bent and stretched, and by $t/t_g = 0.8$ has even undergone noticable reconnection in the high-density region. The matter becomes strongly clumped, with 8 % of the mass at $\log(\rho/\bar{\rho}) > 2$ at $t/t_g = 0.5$, and 62 %(55%) of the mass at $\log(\rho/\bar{\rho}) > 2(3)$ at $t/t_g = 0.8$. In this last frame, a single zone contains 47% of the total mass; because the density in this zone is high enough to make the Jeans length smaller than the grid scale, the simulation is not well-resolved at this point. The $\beta = 10^6$ simulations (not shown) are also initially filamentary, and gradually coagulate due to gravity. The late-time structures

consist of rotationally-supported condensations (with trailing spiral arms); this sort of structure does not develop in the higher-β models because magnetic stresses redistribute angular momentum away from gravitationally-collapsing regions.

3.3. Statistics of Matter Distributions

As described in §3.2, the overall structure in our model clouds evolves in time due to the combined action of gravity, Reynolds stresses, and magnetic stresses. At the same time as the overall structure evolves, the detailed distributions of matter in the models evolves as well. These distributions can be characterised in a variety of ways. We find it informative to consider two related distributions: the fraction of volume dV/V_{tot}, and the fraction of mass $dM/M_{tot} = \rho dV/(\bar{\rho}V_{tot})$, as a function of the logarithmic density enhancement/decrement $\log(\rho/\bar{\rho})$. In Figure 6, we show how these volume and mass distributions appear for the cloud model snapshots portrayed in Figure 5. The values of the volume-averaged and mass-averaged density logarithms

$$\langle \log(\rho/\bar{\rho}) \rangle_V \equiv \sum \frac{\log(\rho/\bar{\rho}) dV(\rho)}{V_{tot}} \tag{10}$$

and

$$\langle \log(\rho/\bar{\rho}) \rangle_M \equiv \sum \frac{\log(\rho/\bar{\rho}) \rho dV(\rho)}{\bar{\rho} V_{tot}} \tag{11}$$

are also indicated, for each distribution.

A number of common features are apparent for all the models shown in Figure 6; these trends apply to our other models, as well: (a) The mass distributions are offset toward larger density than the volume distributions; this simply means that matter is clumped, with the mass-averaged density logarithm larger than the volume-averaged density logarithm. Because most of the volume is at lower-than-average density, while most of the mass is at higher-than-average density, $\langle \log(\rho/\bar{\rho}) \rangle_V$ is negative and $\langle \log(\rho/\bar{\rho}) \rangle_M$ is positive. (b) At earlier times, the distributions are roughly log-normal in shape, while large tails evolve in time. (c) The values of $\langle \log(\rho/\bar{\rho}) \rangle_V$ and $\langle \log(\rho/\bar{\rho}) \rangle_M$ are nearly equal in magnitude, at early times. It is easy to show that for a lognormal distribution, this will be true by definition. (d) Over time, the mass and volume distributions become more separated, for any given model. This is due to the action of gravity increasing the clumping of matter. (e) At the earliest time, before self-gravity becomes important, the $\beta = 0.01$ model has greater density contrast than the $\beta = 0.1, 1$ models.

Given the strong temporal evolution in any of our models, no single distribution characterises its density structure. However, because the density distribution in a real cloud

is one of the most straightforwardly-obtained observables, it is important to investigate in our model clouds how the density distribution depends on the input parameters. If a clear correlation exists between the density distribution and input parameters in our model clouds, then the density distributions in real clouds could potentially be used as a surrogate to determine less-easily observable cloud properties – such as the mean magnetic field strength.

To isolate the effect of the magnetic field in influencing the density distributions in our model clouds, we have chosen to analyze the models early in their evolution, before the effects of gravity become significant. Since the velocity dispersion – corresponding to the kinetic energy in our models – is the other direct observable in real clouds, we select instants in each model cloud's evolution when the kinetic energy has a fixed value; because E_K decays at different rates for different β, these analysis times differ for the different cloud models. To make quantitative comparisons among the models, we evaluate the volume- and mass- averaged density logarithms at times in each model when the kinetic energy has decayed to half of its initial value. These computed values for $\langle \log(\rho/\bar{\rho}) \rangle_V$ and $\langle \log(\rho/\bar{\rho}) \rangle_M$ are listed in the last two columns of Table 1. In a schematic picture of clouds as consisting of denser clumps embedded within a more tenuous interclump medium, we may think of $\langle \log(\rho/\bar{\rho}) \rangle_M$ as describing the magnitude of the positive density contrast in the "clump" component, and $\langle \log(\rho/\bar{\rho}) \rangle_V$ as describing the magnitude of the negative density contrast in the "interclump medium".

Based on the computed values of $\langle \log(\rho/\bar{\rho}) \rangle_V$ and $\langle \log(\rho/\bar{\rho}) \rangle_M$ tabulated, we can make a number of observations. These remarks apply to the set of 27 models with $\beta = 0.01, 0.1, 1$; since the unmagnetized models have unrealistically low field strength, and generally become self-gravitating earlier, we do not consider them here. At fixed E_K and β, we find the variation of the the density contrast with $n_{\rm J}$ is (except for the $\beta = 0.01$, $E_{K,\,init} = 0.25$ models) less than 0.15; thus, these variations are not principally due to gravitational effects (as desired). We also find that for fixed β, the density contrast generally increases with increasing E_K. Finally, we find that at fixed E_K, all except for two models with $\beta = 0.01$ have larger density contrasts than the corresponding $\beta = 0.1, 1$ models at all $n_{\rm J}$.

In Figure 7, we plot the values of the clump and interclump density contrasts *vs* the total magnetic energy density, so that the models with different mean β fall in three separate groups. Within each group, increasing (perturbed) magnetic energy correlates with increasing kinetic energy, accounting for the increase shown in the density contrast toward larger total E_B. The $\beta = 0.1$ points lie quite close to the lines $|\langle \log(\rho/\bar{\rho}) \rangle_{V,M}| = C \log(B^2/(8\pi\bar{\rho}c_s^2))$ with $C = 0.2 - 0.25$, and the $\beta = 0.01$ points lie near the extension of these lines. The $\beta = 1$ points all lie well above these lines, and typically

have density contrasts that fall between the $\beta = 1$ and $\beta = 0.01$ models, at a given E_K.

Physically, the decrease in the density contrast in going from $\beta = 1$ to $\beta = 0.1$ at fixed E_K can probably be attributed to a increase in the effective pressure provided by magnetic fields: for a fixed value of the Mach number $= (2E_K)^{1/2}$, the Alfvén Mach number decreases proportional to $\beta^{1/2}$, and ram-pressure induced density contrast should decrease as the mean magnetic field strength increases. The increase of the density contrast in going from $\beta = 0.1$ to $\beta = 0.01$, on the other hand, is likely the signature of the importance of transverse magnetic fields in compressing the medium. At quasiequilibrium kinks in a strong magnetic field, matter is compressed until the central thermal pressure ρc_s^2 equals the external magnetic pressure $B_\perp^2/8\pi$. For a nonlinear transverse wave, $B_\perp^2/4\pi \sim \bar{\rho} v_\perp^2$, implying $\rho/\bar{\rho} \sim (1/2)(v_\perp/c_s)^2$ at kinks (independent of β). In this situation, the induced density contrast would *not* decrease with increasing mean magnetic field strength. The measured tendency for matter to collect more strongly at nulls of the transverse magnetic field for lower-β simulations may in part owe to the increasing virulence at low β of the decay instability (in which Alfvén waves pump the growth of field-aligned compressive waves and backscattered Alfvén waves; e.g. Sagdeev & Galeev (1969), Goldstein (1978)), which may cause the lowest-β models to approach the kinked-field state more rapidly. We discuss potential implications of our results on density contrast in §4.3 .

4. Discussion

4.1. Summary and comparison with other work

In this paper, we present the results of a suite of 2.5-dimensional simulations following the evolution of cloud models with dynamical parameters comparable to those believed to hold in Galactic molecular clouds. Our models, which assume cold, isothermal conditions, are initiated with random, turbulent velocity fields, and include the effects of self-gravity and magnetic forces. We parameterize the importance of magnetic fields by $\beta = c_s^2/v_A^2$ (see eq. 5), and the importance of self-gravity by the Jeans number $n_J \equiv L/L_J$ (see eq. 2). We follow the evolution of cloud models over time as they dissipate kinetic energy in shocks, and as the clumps, sheets, and filaments formed by the action of magnetic and Reynolds stresses coalesce under their own self-gravity.

In §3.1, we compare for different models the times needed for clouds to become gravitationally bound, and the times needed to reach a state with stronger gravitational binding than a thin sheet. We find that only the models which are magnetically subcritical ($\beta^{1/2} n_J < 1/\pi$) survive gravitational collapse for times significantly longer than $t = t_g$;

in §4.2 below we comment on the implications of these results. We have also compared the evolution of kinetic energies, and perturbed magnetic energies, among our models. In examining the amplification of the perturbed magnetic field, we found that the peak value of δE_B attains higher amplitudes, and occurs at earlier times, for the lower-β models (see eq. 9). To quantify the decay of turbulent energy, we compare the kinetic energy after a cloud crossing time (i.e. an "eddy turnover time") with the initial kinetic energy. We find, for models that have not become strongly self-gravitating at this time, that the kinetic energy is a fraction 0.26-0.29, 0.33-0.36, 0.32-0.46, and 0.42-0.48 of the initial value, for $\beta = 10^6, 1, 0.1$, and 0.01, respectively. Thus, while the models with stronger fields have lowered dissipation, the effect occurs at a level less than a factor of two, for realistic field strengths. Although the simulations of MacLow et al (1998) and Padoan & Nordlund (1997) have somewhat different parameters, they also find kinetic energy reduced to 0.3-0.5 of the initial value, after one crossing time, and differences of no more than a factor two between their low-β and high-β cases. On the other hand, the dissipation in our set of 1D models (Paper I) was much less than in the present set, because the 1D simulations' initial velocity fields were purely transverse, and the model symmetry inhibited dissipation. Since real clouds are probably much more similar to the 2.5D and 3D models than the 1D models, we conclude that realistic turbulent dissipation times $E_K/\dot{E}_K$ are not likely to be more than twice the cloud fluid crossing times – i.e., $\lesssim 10$ Myr – for any likely value of the mean magnetic field. Although the hope of substantially lowering turbulent dissipation rates in molecular clouds by including magnetic fields (Arons & Max (1975)) may not be fully realized, the feedback provided by star formation (e.g. Norman & Silk (1980)) on timescales comparable to the turbulent decay (see §4.2) may yet allow a quasi-steady state to exist (e.g. McKee (1989), Gammie & Ostriker (1996)).

We present, in §3.2, snapshots showing density contours, magnetic field lines, and the velocity field in cloud models with varying levels of the mean magnetic field strength (i.e. β). All models show highly inhomogeneous density structure well before gravity becomes important in the dynamics. However, as gravity becomes important, the matter in subcritical clouds collapses into sheets, whereas in supercritical clouds it collapses into rounder clumps (and reaches much higher densities). In §4.2 below, we summarize our results (based on the analysis in §3.3) on the distributions of matter in our models, and comment on implications for interpreting the clumpy structure of observed clouds.

4.2. Implications for cloud support and the initiation of star formation

Observed molecular clouds have column densities in the range $N_{H_2} = 3 - 10 \times 10^{21} \mathrm{cm}^{-2}$ (e.g. Larson (1981), Myers & Goodman (1988b), Blitz (1993)). The corresponding magnetic field strengths required for such clouds to be cross-field ("magneto-Jeans") stable (see §2.2) are in the range $7 - 24\mu$G, within the range of field strengths that are believed to prevail on the large scale in molecular clouds (§1). However, typical observed field strengths fall short of the value $23 - 77\mu$G which would be required to render the same clouds magnetically subcritical; i.e., able to resist gravitational fragmentation if all of the cloud's mass is collected into a sheet, rather than homogeneously filling a volume with sides comparable to its lateral extent. In the simulations presented in this paper, we show that regardless of the initial turbulent energy content of our model clouds, only those clouds which are magnetically subcritical remain uncollapsed throughout the simulations for times exceeding $1.5t_g$ – corresponding to $\approx$ 15Myr for typical conditions. In fact, the only supercritical clouds that survive uncollapsed beyond $t_g \sim$ 10Myr are relatively small ($n_{\mathrm{J}} = 2$, $L \sim$ 4pc) and magneto-Jeans stable. Very low magnetization clouds collapse in $0.5t_g \sim$ 5Myr; this puts a lower limit on the collapse time for supercritical clouds. Since the Milky Way molecular clouds contianing most of the mass are probably not magnetically subcritical and have sizes exceeding $\sim$ 4pc, our simulations imply that they cannot survive for periods longer than $5 - 10$Myr without some of part of their interiors becoming strongly gravitationally bound, and, we expect, beginning to form stars. We regard this as one of the two main conclusions of the present work.

Observationally-based estimates of the time to initiate star formation are necessarily indirect, and subject to major uncertainty. Based on Williams & McKee (1997)'s analysis of the joint distributions of OB associations and GMCs (assuming all molecular material is associated with discrete clouds with a spectrum of masses $dN/dM \propto M^{-1.6}$), if star formation is equally distributed among all clouds, then roughly 80% of the Galactic molecular material would reside in clouds containing one or more OB stars. If we take this fraction as representing the portion of a cloud's life during which it contains an OB association, and use 20 Myr (Blaauw (1991)) as the typical observed lifetime of associations, this implies that associations form in clouds after 20% of their 25 Myr lifetimes, essentially as soon as our models predict that star formation is initiated in supercritical clouds (5-10 Myr). On the other hand, even in the largest existing cloud catalog (Solomon et al (1987)) created for the inner Galaxy, $\sim$ 60% of molecular material was not actually assigned to discrete clouds, perhaps because it has not been sufficiently warmed internally by massive

stars to stand out above the background (Solomon & Rivolo (1989)).[5] If this cold material is in clouds with the same mass distribution as the warm clouds, we would infer that 60% of a cloud's lifetime passes before OB stars form; a period of > 20Myr must therefore be spent in forming exclusively low mass stars, if the clouds are supercritical and the first stars form after $5 - 10$Myr. If, on the other hand, much of the cold molecular material is distributed in small, subcritical clouds that never make OB associations, then OB star formation in supercritical clouds would again be inferred to commence soon after clouds first begin to have portions of their interior collapse.

Based on the above discussion, the range of star formation scenarios permitted by observations is fairly large at present. However, the planned high-resolution Boston University/FCRAO Galactic Ring Survey in ^{13}CO and CS (M. Heyer, personal communication) should considerably constrain the molecular cloud distribution function, and correspondingly constrain the possible evolutionary scenarios for star formation and cloud destruction. This, in turn, should allow us better to evaluate the conclusions of this paper on the time to initiate star formation in magnetized GMCs.

4.3. Implications for clumpy structure of GMCs

The other finding which we would like to highlight concerns the distribution of density found in our simulated clouds, and the potential to use observed density distributions in real clouds as a diagnostic of the magnetic field strength. We find, in concurrence with other recent work on isothermal cloud models, that the shapes of the density distribution functions before self-gravity becomes important are roughly log-normal. Our own analysis of density distributions presented in §3.3, however, primarily focuses not on the shape of the density distribution function, but instead on the values of volume-weighted and mass-weighted means of the logarithmic density, $\langle \log(\rho/\bar{\rho}) \rangle_V$ and $\langle \log(\rho/\bar{\rho}) \rangle_M$. These represent the magnitudes, respectively, of the (negative) density contrast in the tenuous interclump region, and the (positive) density in the cloud clumps, relative to the mean cloud density. For a lognormal distribution, $\langle \log(\rho/\bar{\rho}) \rangle_V$ and $\langle \log(\rho/\bar{\rho}) \rangle_M$ will be equal in magnitude and opposite in sign; this result holds for most of our models, when analyzed at early times. We find that the values of the mean density contrast depend both on the amplitude of the turbulence (i.e. the value of E_K), and on the strength of the mean

[5]For a fixed number of OB associations, reducing the fraction of clouds containing massive stars increases the photoevaporation rate for those clouds that *do* contain associations, making estimates of cloud destruction timescales more consistent with observed OB association lifetimes (Williams & McKee (1997)).

magnetic field and its perturbations (i.e. the value of E_B). Specifically, we find that for a given β, the density contrast increases with E_K, and that virtually all of the more strongly-magnetized ($\beta = 0.01$) models have larger mean density contrast than the more weakly-magnetized ($\beta = 1, 0.1$) models with the same value of E_K. We also find that the $\beta = 1$ models generally have higher density contrast than the $\beta = 0.1$ models. Given the limitations of the current set of simulations, we did not attempt to formulate a more general theory for the relationship between the mean density contrast and the values of E_K and β. We defer this much-desired goal until the completion of surveys of 2D and 3D forced, non-self-gravitating MHD turbulence which are now underway.

While follow-up studies are clearly needed, it is nevertheless tempting to compare our present results with observations. Molecular clouds are often characterized as consisting of clumps embedded in an interclump medium, with a fraction $\theta_H \equiv M_H/M_{tot}$ of the mass, and $f_H = V_H/V_{tot}$ of the volume contained in the high density component ($\rho_H/\bar{\rho} = \theta_H/f_H$), and the remainder of the mass and volume dispersed in a low-density component ($\rho_L/\bar{\rho} = (1-\theta_H)/(1-f_H)$). From ^{13}CO maps of Orion A and the Rosette clouds, Bally et al (1987) and Williams, Blitz, & Stark (1995) estimate $\theta_H = 0.75, 0.77$ and $f_H = 0.1, 0.08$, respectively. With this simple clump/interclump structure, we use

$$\langle \log(\rho/\bar{\rho}) \rangle_V = f_H \log(\rho_H/\bar{\rho}) + (1-f_H) \log(\rho_L/\bar{\rho}) \tag{12}$$

and

$$\langle \log(\rho/\bar{\rho}) \rangle_M = \theta_H \log(\rho_H/\bar{\rho}) + (1-\theta_H) \log(\rho_L/\bar{\rho}). \tag{13}$$

to compute density contrast magnitudes of $\langle \log(\rho/\bar{\rho}) \rangle_V = -0.4, -0.5$ and $\langle \log(\rho/\bar{\rho}) \rangle_M = 0.5, 0.6$ for the two clouds. The clumps defined in these observations are not believed to be self-gravitating; thus, it is fair to compare to the model density contrast magnitudes computed in §3.3. Of the present models with $\beta = 1, 0.1, 0.01$ (corresponding to $B_0 \sim 1.4, 4.4, 14.4\mu$G), Figure 7 shows that only the $\beta = 0.01$ simulations have density contrasts as large as ± 0.5; thus, the stronger-field cases seem to be in better agreement with observations, when taken at face value. As argued in §3.3, both $\beta > 1$ and $\beta < 0.01$ could yield larger density contrast, although the former (corresponding to sub-μG fields) is unlikely to exist in the present-day Galaxy. The implication that $B_0 \gtrsim 15\mu$G is far from definitive, but demonstrates the potential to develop magnetic field diagnostics from more readily observed cloud properties such as the clump/interclump density contrast. We view this as an an important direction for future research.

This work was supported in part by NASA grant NAG 53840.

REFERENCES

Arons, J. & Max, C. E. 1975, ApJ, 196, L77

Bally, J., Langer, W. D., Stark, A. A., & Wilson, R. W. 1987, ApJ, 312, L45

Blitz, L. 1993, in Protostars and Planets III, ed. E. Levy & J. Lunine (Tucson: University of Arizona Press), p. 125

Blaauw, A. 1991, in The Physics of Star Formation, Eds. C. J. Lada & N. D. Kylafis (Dordrecht: Kluwer)

Chandrasekhar, S. & Fermi, E. 1953, ApJ, 118, 116

Crutcher, R. M., Troland, T. H., Goodman, A. A., Heiles, C., Kazes, I., & Myers, P. C., ApJ, 407, 175

Crutcher, R. M. 1998, in Interstellar Turbulence, Proceedings of the 2nd Guillermo Haro Conference, Eds. Franco, J. & Carraminana, A., Cambridge University Press

Elmegreen, B. G. 1997, ApJ, 480, 674

Evans, C. R., & Hawley, J. F. 1988, ApJ, 332, 659

Falgarone, E., Puget, J. L., & Pérault, M. 1992, A&A, 257, 715

Falgarone, E., Panis, J.-F., Heithausen, A., Perault, M., Stutzki, J., Puget, J.-L., Bensch, F. 1998, A&A, 331, 669

Gammie, C. F. & Ostriker, E. C. 1996, ApJ, 466, 814 (Paper I)

Goldsmith, P. F. 1987, in Interstellar Processes, eds. D.J. Hollenbach and H.A. Thronson (Dordrecht: Reidel), p. 51

Goldstein, M.L. 1978, ApJ, 219, 700

Goodman, A. A., Bastien, P., Myers, P. C., & Menard, F. (1990), ApJ, 359, 363

Goodman, A. A., & Heiles, C. 1994, ApJ, 424, 208

Goodman, A. A., Jones, T. J., Lada, E. A., & Myers, P. C. 1995, ApJ, 448, 748

Hawley, J.F., Gammie, C.F., & Balbus, S. A. 1996, ApJ, 464, 690

Heiles, C., Goodman, A. A., McKee, C. F., & Zweibel, E. G. 1993, in Protostars and Planets III, ed. E. Levy & J. Lunine (Tucson: University of Arizona Press), p. 279

Lada, C. J., Lada, E. A., Clemens, D. P., & Bally, J. 1994, ApJ, 429, 694

Lada, C. J., Alves, J., & Lada, E. A. 1998, in preparation

Larson, R. B. 1981, MNRAS, 194, 809

MacLow, M. M., Klessen, R. S., Burkert, A., Smith, M. D., & Kessel, O. 1998, preprint

McKee, C. F. 1989, ApJ, 345, 782

McKee, C. F., Zweibel, E. G., Goodman, A. A., & Heiles, C. 1993, in Protostars and Planets III, ed. E. Levy & J. Lunine (Tucson: University of Arizona Press), p. 327

Menneguzzi, M., Frisch, U.,& Pouquet, A. 1981 PRL, 47, 1060

Mouschovias, T., & Spitzer, L. 1976, ApJ, 210, 326

Mouschovias, T., in The Physics of Star Formation and Early Stellar Evolution, Eds. C. J. Lada & N. D. Kylafis (Dordrecht: Kluwer), p. 61

Myers, P. C., & Goodman, A. A. 1988a, ApJ, 326, L27

Myers, P. C., & Goodman, A. A. 1988b, ApJ, 329, 392

Nordlund, A., & Padoan, P 1998, in Interstellar Turbulence, Proceedings of the 2nd Guillermo Haro Conference, Eds. Franco, J. & Carraminana, A., Cambridge University Press

Norman, C., & Silk, J. 1980, ApJ, 238, 158

in Star Formation Near and Far, Eds. S. Holt & L. Mundy, Woodbury NY: AIP Press, p. 51

Padoan, P., & Nordlund, A. 1997, preprint

Padoan, P., Jones, B. T., & Nordlund, A. P. 1997, ApJ, 474, 730

Passot, T., Vazquez-Semadeni, E., & Pouquet, A. 1995, ApJ, 455, 536

Passot, T., & Vazquez-Semadeni, E. 1998, Phys Rev E, submitted

Sagdeev, R. Z., & Galeev, A. A. 1969, Nonlinear Plasma Theory (New York: W. A. Benjamin)

Scalo, J., Vazquez-Semadeni, E., Chappell, D., & Passot, T. 1998, ApJ, submitted

Schleuning, D. A. 1998, ApJ, 493, 811

Shu, F.H., Adams, F.C. & Lizano, S. 1987, ARA&A, 25, 23

Solomon, P. M., Rivolo, A. R., ApJ, 339, 919

Solomon, P. M., Rivolo, A. R., Barrett, J., & Yahil, A. 1987, ApJ, 319, 730w

Stone, J. M., in "Interstellar Turbulence," eds. J. Franco & A. Carraminana (Cambridge U. Press)

Stone, J. M. & Norman, M. L. 1992a, ApJSupp, 80, 753

Stone, J. M. & Norman, M. L. 1992b, ApJSupp, 80, 791

Tomisaka, K., Ikeuchi, S., & Nakamura, T. 1988, ApJ, 335, 239

Troland, T. H., Crutcher, R. M., Goodman, A. A., Heiles, C., Kazes, I., & Myers, P. C. 1996, ApJ, 471, 302

Vazquez-Semadeni, E., Passot, T., & Pouquet, A. 1996, ApJ, 473, 881

Williams, J. P., & McKee, C. F. 1997, ApJ, 476, 166

Williams, J. P., Blitz, L. & Stark, A. A. 1995, ApJ, 451, 252

This preprint was prepared with the AAS LaTeX macros v4.0.

Table 1. Evolutionary Characteristics of Model Clouds

β	n_J	$E_{K,init}$	$\frac{t_{bind}}{t_g}$ [a]	$\frac{t_{condense}}{t_g}$ [b]	$\frac{E_K(t_{cr})}{E_{K,init}}$ [c]	$\frac{\delta E_B}{E_K(t_{cr})}$ [c]	$\langle log(\rho/\bar{\rho})\rangle_V$ [d]	$\langle log(\rho/\bar{\rho})\rangle_M$ [e]
0.01	2	25	>1.0	>1.0	0.46	0.39	-0.4	0.3
0.01	2	50	>1.7	>1.7	0.47	0.31	-0.5	0.4
0.01	2	100	>1.5	>1.5	0.42	0.39	-0.5	0.5
0.01	3	25	0.9	>1.0	0.45	0.40	-0.5	0.5
0.01	3	50	>1.5	>1.5	0.46	0.31	-0.4	0.4
0.01	3	100	>1.5	>1.5	0.42	0.39	-0.4	0.4
0.01	4	25	0.7	0.8	0.48	0.33	-0.7	0.9
0.01	4	50	0.9†	>0.8	0.47	0.32	-0.5	0.5
0.01	4	100	>0.8	>0.8	0.42	0.39	-0.5	0.5
0.1	2	25	1.4	1.2	0.45	0.24	-0.2	0.2
0.1	2	50	1.6†	1.5	0.36	0.51	-0.3	0.3
0.1	2	100	1.6†	1.4	0.32	0.61	–	–
0.1	3	25	0.8*	0.8*	0.46	0.28	-0.2	0.3
0.1	3	50	1.0	0.9	0.36	0.50	-0.3	0.3
0.1	3	100	0.9†	0.8*	0.32	0.62	-0.3	0.3
0.1	4	25	0.6*	0.6*	0.50	0.49	-0.2	0.3
0.1	4	50	0.6*	0.6*	0.41	0.49	-0.3	0.3
0.1	4	100	0.6†	0.6	0.32	0.62	-0.3	0.3
1	2	25	0.9	0.8	0.33	0.54	-0.2	0.3
1	2	50	1.1	0.9	0.34	0.38	-0.3	0.3
1	2	100	1.0*	0.7	0.36	0.25	–	–
1	3	25	0.5*	0.5*	0.39	0.52	-0.3	0.3
1	3	50	0.7*	0.6*	0.34	0.39	-0.3	0.3
1	3	100	0.7*	0.7*	0.35	0.25	-0.4	0.4
1	4	25	0.5	0.5	0.70	0.52	-0.4	0.4
1	4	50	0.6	0.5	0.37	0.40	-0.4	0.4
1	4	100	0.6*	0.6*	0.35	0.26	-0.4	0.4
10^6	2	25	0.6	0.6	0.29	9×10^{-6}	-0.4	0.4
10^6	2	50	0.5	0.5	0.27	5×10^{-6}	-0.4	0.4
10^6	3	25	0.5	0.6	0.32	9×10^{-6}	-0.5	0.5
10^6	3	50	0.5	0.6	0.26	6×10^{-6}	-0.5	0.5
10^6	4	25	0.5	0.6	0.58	4×10^{-6}	-0.8	1.0
10^6	4	50	0.5	0.6	0.29	1×10^{-5}	-0.6	0.6

[a] t_{bind} is defined as the time at which $E_K + E_G + \delta E_B = 0$

[b] $t_{condense}$ is defined as the time at which $E_G/E_{G,sheet} = 1$ where $E_{G,sheet} = -[(n_J^2\pi^2/6) - 1]$.

[c] Evaluated at the crossing time $t_{cr} \equiv L/(2E_{K,\,init})^{1/2}$

[d] Volume-weighted average of $\log(\rho/\bar{\rho})$, evaluated at the time when $E_K = E_{K,init}/2$ (see text).

[e] Mass-weighted average of $\log(\rho/\bar{\rho})$, evaluated at the time when $E_K = E_{K,init}/2$ (see text).

† Extrapolated

* Self-gravity has become unresolved at the grid scale before this measurement is made

Fig. 1.— Evolution of the total specific energy $E_{tot}/c_s^2 \equiv (E_K + \delta E_B + E_G)/c_s^2$ for all models. Solid, dotted, and dashed curves have $n_J = 2, 3$, and 4, respectively.

Fig. 2.— Evolution of the specific kinetic energy for all models. Solid, dotted, and dashed curves have $n_J = 2, 3$, and 4, respectively.

Fig. 3.— Evolution of the perturbed magnetic energy (per unit mass) for all models. Solid, dotted, and dashed curves have $n_J = 2, 3$, and 4, respectively.

Fig. 4.— Density snapshots of the $\beta = 0.01$, $n_J = 3$, $E_{K,\ init} = 50$ model cloud at temporal intervals of $0.1t_g$. Density contours are at equal intervals in $\log(\rho/\bar{\rho}) = 0, 0.5, 1., ...$

Fig. 5.— Comparative evolution of cloud models with different magnetization. Left, center, and right columns have $\beta = 0.01$, 0.1, and 1, respectively. $E_{K,\ init} = 50$ and $n_J = 3$ for all three runs. Snapshots at times $t/t_g = 0.2, 0.5,$ and0.8 show density contours ($\log(\rho/\bar{\rho}) =$ 0-0.9:dark blue, 1-1.9:light blue, 2-2.9:yellow, 3-5:magenta), velocity vectors (red), and magnetic field lines (green).

Fig. 6.— Comparative evolution of density distributions in cloud models with different magnetization. Same parameters and intervals as in Fig. 5. The solid histograms show the distribution of volume dV/V_{tot}, and the dashed histograms show the distribution of mass dM/M_{tot}, as a function of density, for each snapshot. The numbers in the upper-right of each panel indicate the values of the means $\langle \log(\rho/\bar{\rho}) \rangle_M$ (top) and $\langle \log(\rho/\bar{\rho}) \rangle_V$ (bottom) for each distribution.

Fig. 7.— Mass-averaged (upper points) and volume-averaged (lower points) density contrast in model clouds when $E_K = 0.5E_{K,\ init}$, as a function of total magnetic energy. Vertical dashed lines separate results from models with $\beta = 1, 0.1, 0.01$. Point type denotes Jeans number n_J: triangles, squares, pentagons for $n_J = 2, 3, 4$, respectively. The dotted lines indicate logarithmic slopes of ± 0.2 and ± 0.25.

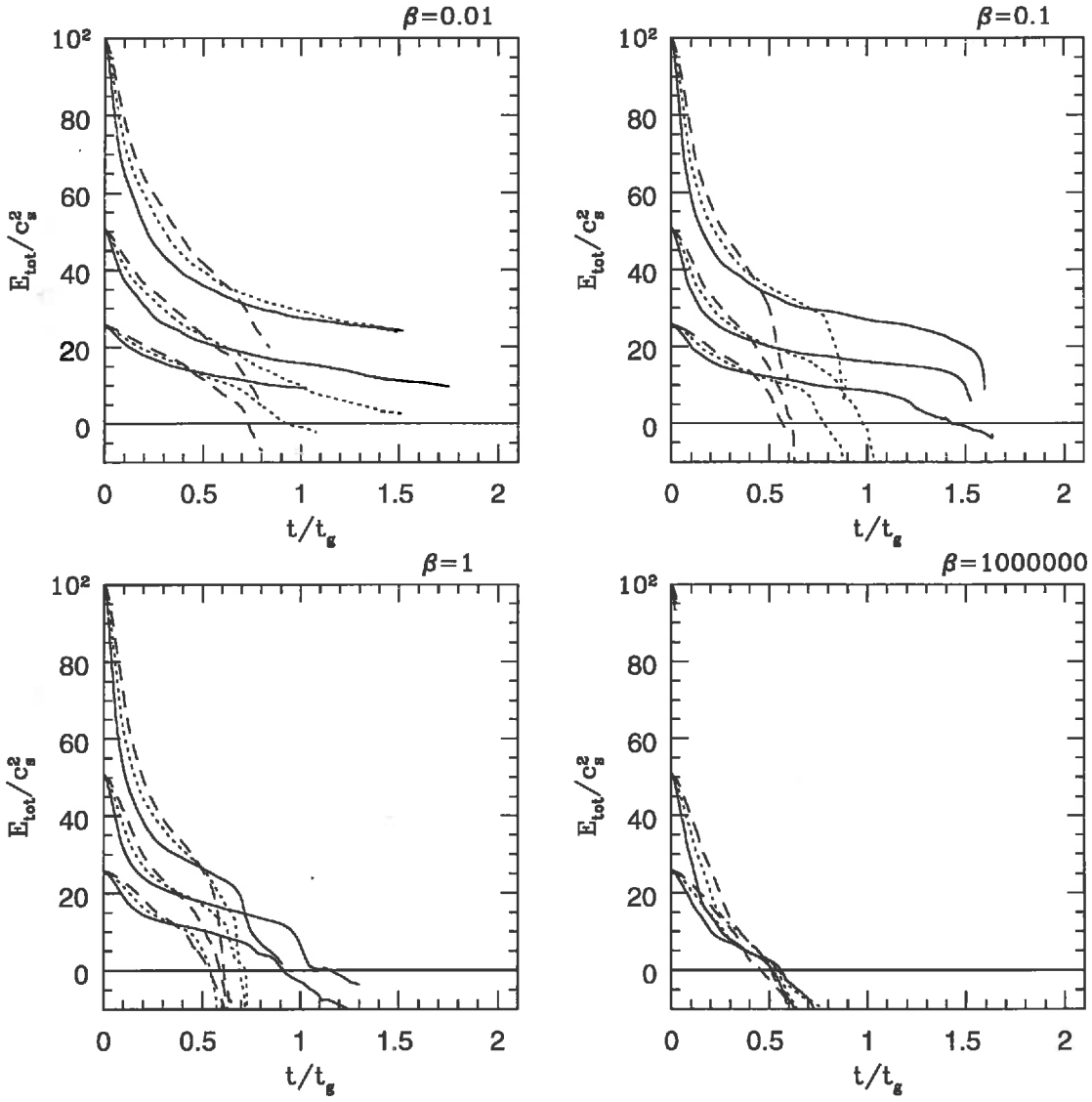

Fig. 1.— Evolution of the total specific energy $E_{tot}/c_s^2 \equiv (E_K + \delta E_B + E_G)/c_s^2$ for all models. Solid, dotted, and dashed curves have $n_J = 2, 3$, and 4, respectively.

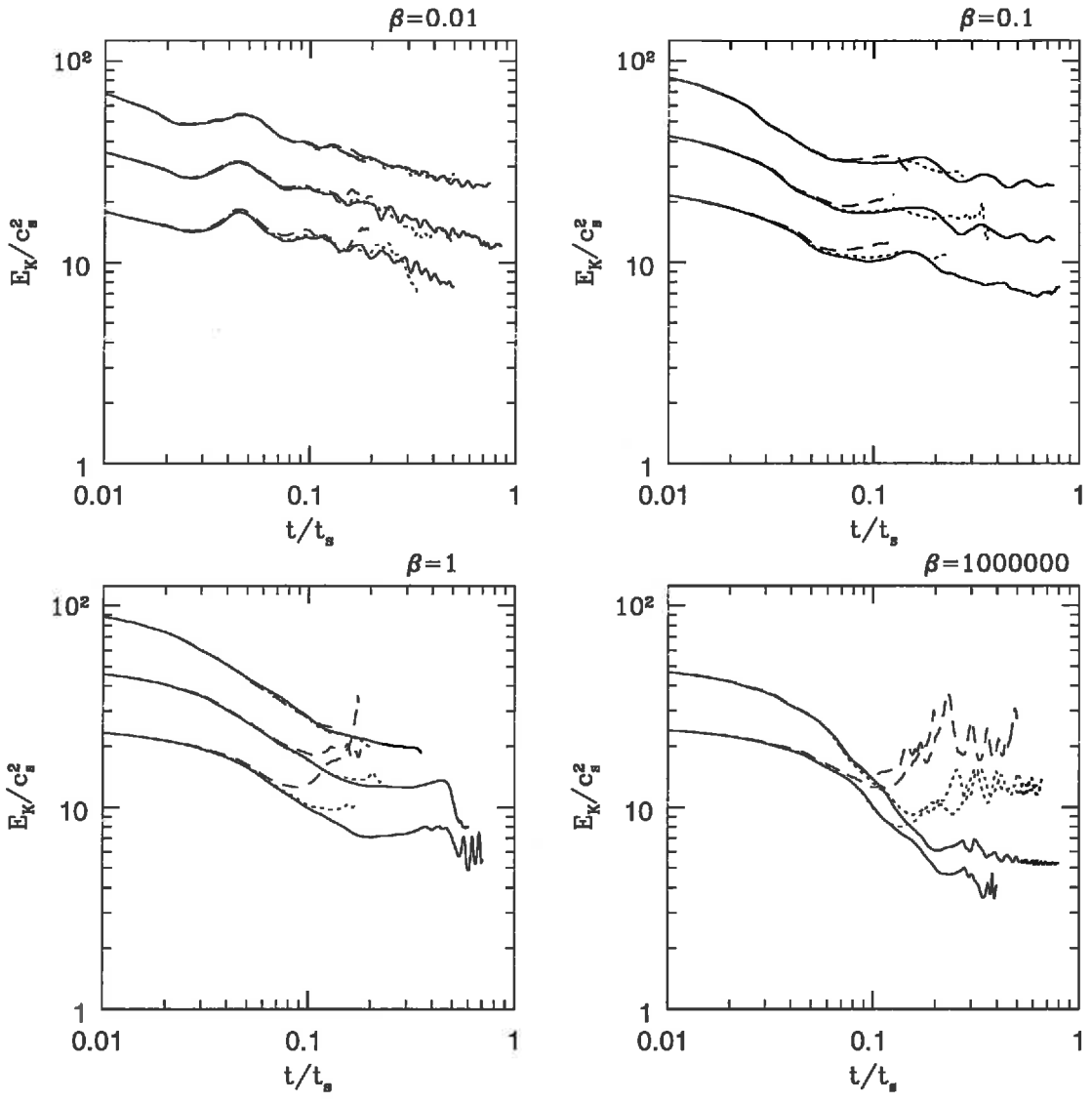

Fig. 2.— Evolution of the specific kinetic energy for all models. Solid, dotted, and dashed curves have $n_J = 2, 3$, and 4, respectively.

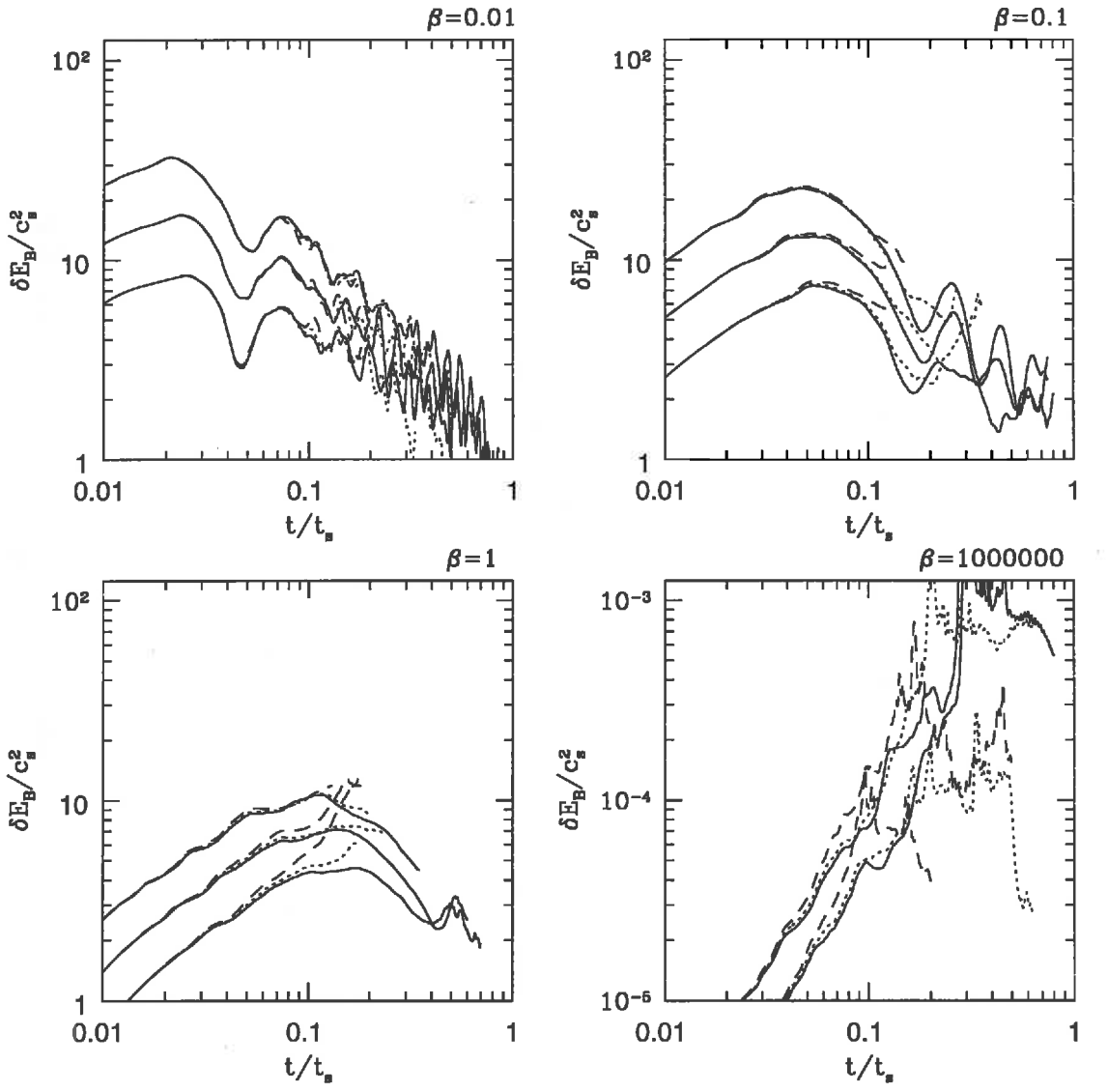

Fig. 3.— Evolution of the perturbed magnetic energy (per unit mass) for all models. Solid, dotted, and dashed curves have $n_J = 2, 3$, and 4, respectively.

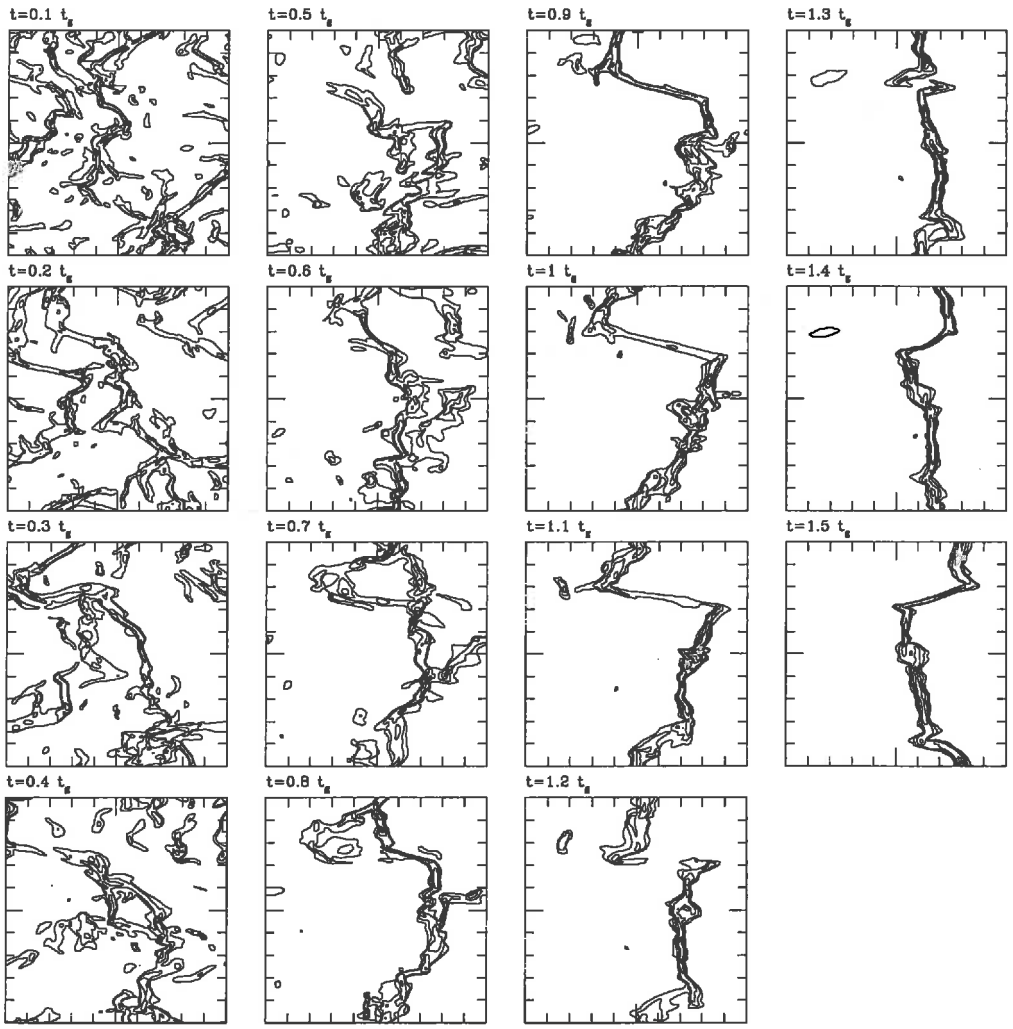

Fig. 4.— Density snapshots of the $\beta = 0.01$, $n_J = 3$, $E_{K,\ init} = 50$ model cloud at temporal intervals of $0.1t_g$. Density contours are at equal intervals in $\log(\rho/\bar{\rho}) = 0, 0.5, 1., ...$

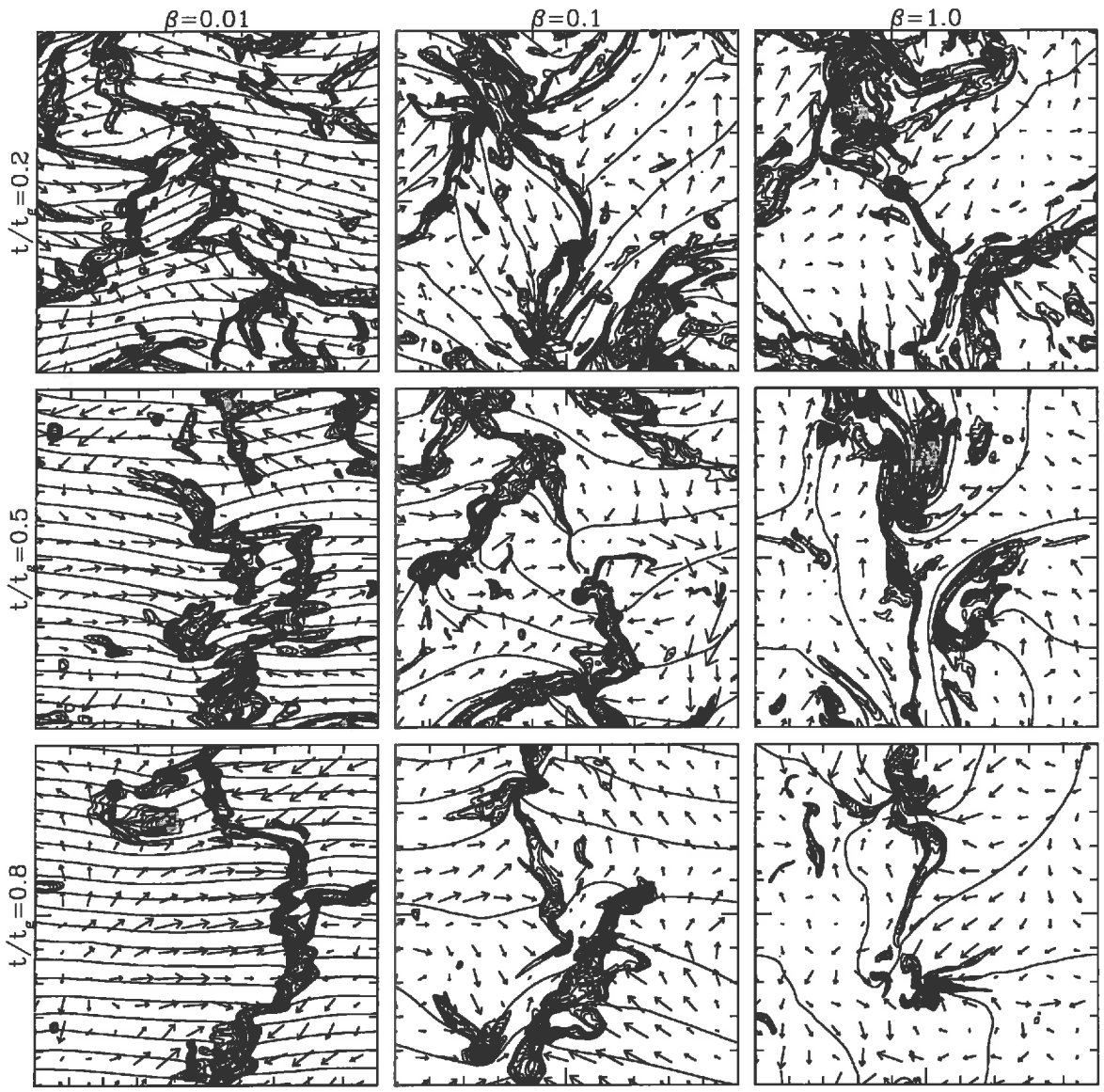

Fig. 5.— Comparative evolution of cloud models with different magnetization. Left, center, and right columns have $\beta = 0.01$, 0.1, and 1, respectively. $E_{K,\ init} = 50$ and $n_J = 3$ for all three runs. Snapshots at times $t/t_g = 0.2, 0.5,$ and0.8 show density contours ($\log(\rho/\bar{\rho}) =$ 0-0.9:dark blue, 1-1.9:light blue, 2-2.9:yellow, 3-5:magenta), velocity vectors (red), and magnetic field lines (green).

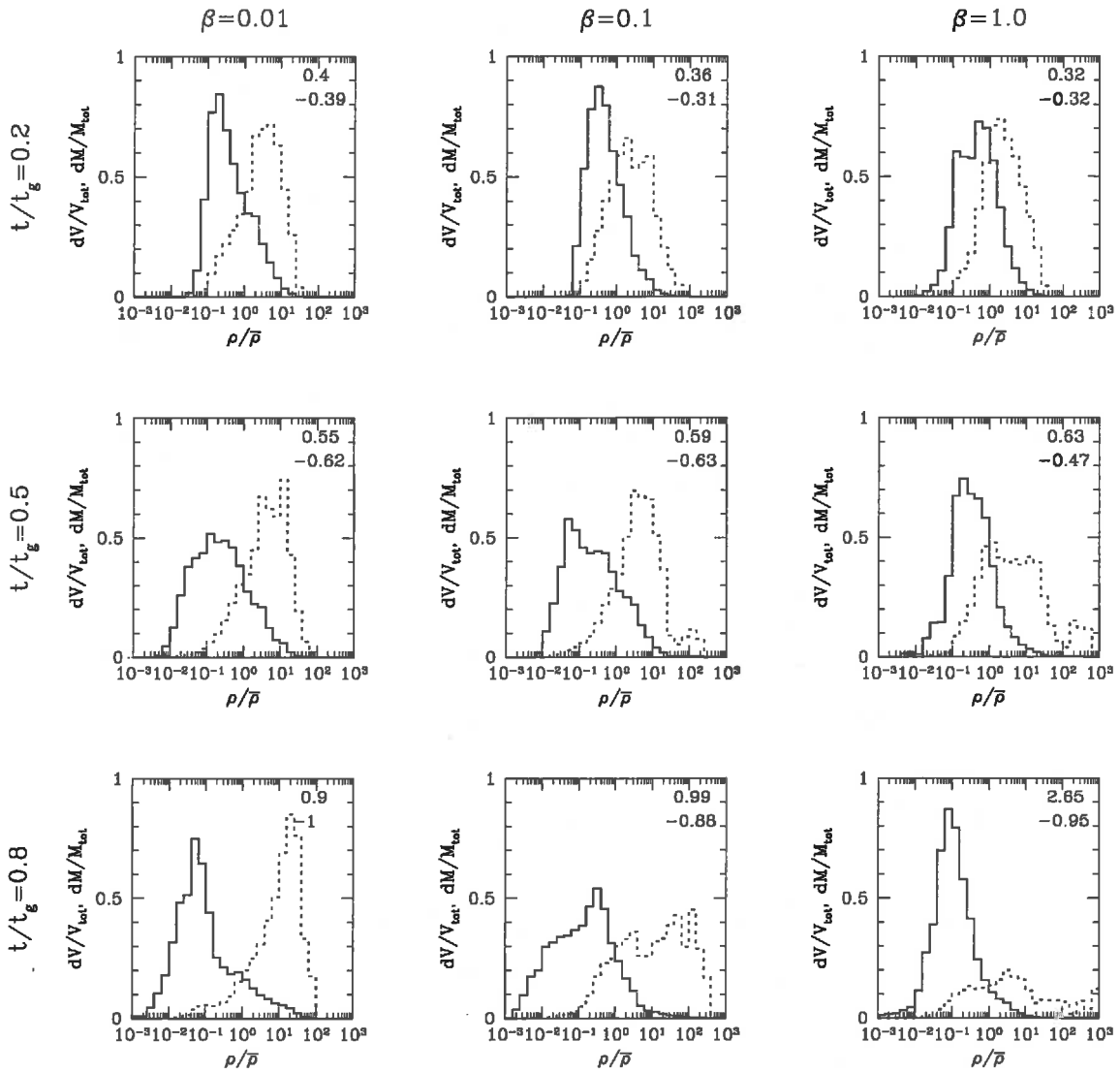

Fig. 6.— Comparative evolution of density distributions in cloud models with different magnetization. Same parameters and intervals as in Fig. 5. The solid histograms show the distribution of volume dV/V_{tot}, and the dashed histograms show the distribution of mass dM/M_{tot}, as a function of density, for each snapshot. The numbers in the upper-right of each panel indicate the values of the means $\langle \log(\rho/\bar{\rho}) \rangle_M$ (top) and $\langle \log(\rho/\bar{\rho}) \rangle_V$ (bottom) for each distribution.

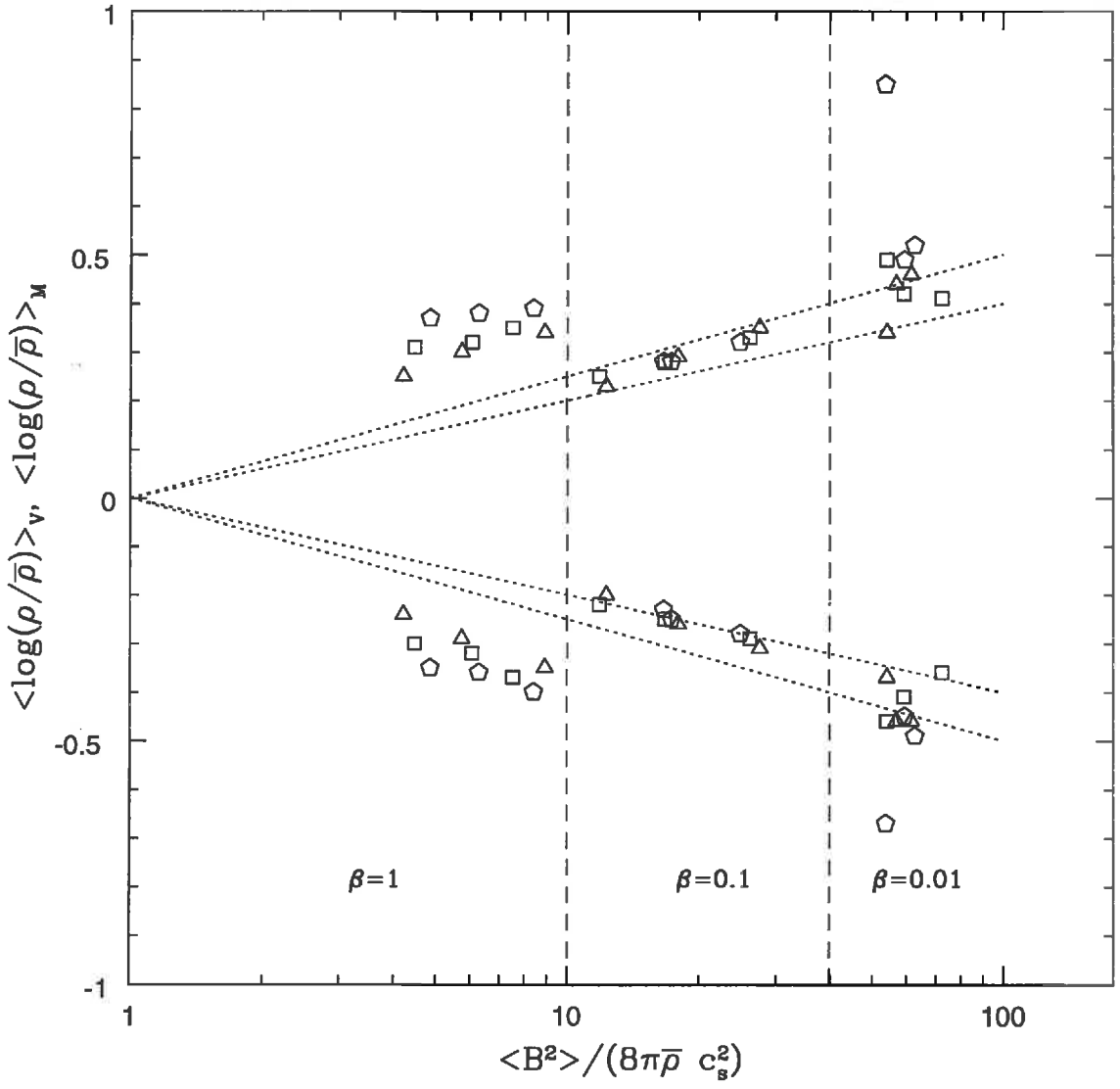

Fig. 7.— Mass-averaged (upper points) and volume-averaged (lower points) density contrast in model clouds when $E_K = 0.5E_{K,\,init}$, as a function of total magnetic energy. Vertical dashed lines separate results from models with $\beta = 1, 0.1, 0.01$. Point type denotes Jeans number n_J: triangles, squares, pentagons for $n_J = 2, 3, 4$, respectively. The dotted lines indicate logarithmic slopes of ± 0.2 and ± 0.25.

Recent Newton Institute Preprints

NI97025-NQF **P van Baal**
Intermediate volumes and the role of instantons

NI97026-NQF **CJ Houghton, NS Manton and PM Sutcliffe**
Rational maps, monopoles and skyrmions
hep-th/9705151; Nuclear Physics B510 [PM] (1998) 507-537

NI97027-NQF **PS Howe, E Sezgin and PC West**
Aspects of superembeddings
hep-th/9705903

NI97028-NQF **CM Hull**
Gravitational duality, branes and charges
hep-th/9705162; Nucl.Phys. B509 (1998) 216-251

NI97029-NQF **M Abou Zeid and CM Hull**
Instrinsic geometry of D-branes
hep-th/9704021; Phys.Lett. B404 (1997) 264-270

NI97030-NQF **CP Bachas, MR Douglas and MB Green**
Anomalous creation of branes
hep-th/9705074

NI97031-RAG **M Broué, G Malle and J Michel**
Complex reflection groups, braid groups, Hecke algebras

NI97032-NQF **D Zwanziger**
Renormalization in the Coulomb gauge and order parameter for confinement in QCD

NI97033-NQF **E Shuryak and A Zhitnisky**
The gluon/charm content of the $\eta\prime$ meson and instantons
hep-ph/9706316; Phys.Rev. D57 (1998) 2001-2004

NI97035-RAG **K Magaard and G Malle**
Irreducibility of alternating and symmetric squares

NI97036-STA **N Linden and S Popescu**
On multi-particle entanglement

NI97037-NNM **M Studeny and RR Bouckaert**
On chain graph models for description of conditional independence structures

NI97038-RAG **M Geck and G Malle**
On special pieces in the unipotent variety

NI97039-NNM **SP Luttrell**
A unified theory of density models and auto-encoders
DERA report DERA/CIS/CIS5/651/FUN/STIT/5-4 31 October 1997

NI97040-NNM **CKI Williams and D Barber**
Bayesian Classification with Gaussian Processes

NI97041-NNM **TS Richardson**
Chain graphs and symmetric associations

NI97042-NNM **A Roverato and J Whittaker**
An importance sampler for graphical Gaussian model inference

NI97043-DQC **MR Haggerty, JB Delos, N Spellmeyer et al**
Extracting classical trajectories from atomic spectra

NI97044-DQC **S Zelditch**
Large level spacings for quantum maps in genus zero

NI97045-DQC **U Smilansky**
Semiclassical quantization of maps and spectral correlations

NI97046-DQC **IY Goldscheid and BA Khoruzhenko**
Distribution of Eigenvalues in non-Hermitian Anderson models
Phys. Rev. Lett. 80 (1998) No.13, 2897-2900

NI97047-DQC **G Casati, G Maspero and DL Shepelyansky**
Quantum fractal Eigenstates

NI98001-STA **N Linden and S Popescu**
Non-local properties of multi-particle density matrices

NI98002-AMG **J-L Colliot-Thélène**
Un principe local-global pour les zéro-cycles sur les surfaces fibrés en coniques au-dessus d'une courbe de genre quelconque

NI98003-AMG **RGE Pinch and HPF Swinnerton-Dyer**
Arithmetic of diagonal quartic surfaces, II

NI98004-AMG **DR Heath-Brown**
The solubility of diagonal cubic diophantine equations

NI98005-AMG **B Poonen and M Stoll**
The Cassels-Tate pairing on polarized Abelian varieties

NI98006-AMG **P Parimala and V Suresh**
Isotropy of quadratic forms over function fields of curves over p-adic fields

NI98007-AMG **E Peyre**
Application of motivic complexes to negligible classes

NI98008-AMG **E Peyre**
Torseurs universels et méthode du cercle

NI98009-RAG **JA Green**
Discrete series characters for $GL(n, q)$

NI98010-DQC **K Zyczkowski**
On the volume of the set of mixed entangled states

NI98011-DQC **K Zyczkowski**
Monge distance between quantum states

NI98012-DAD **JA Sellwood, RW Nelson and S Tremaine**
Resonant thickening of disks by small satellite galaxies

NI98013-DAD **GI Ogilvie and SH Lubow**
The effect of an isothermal atmosphere on the propagation of three-dimensional waves in a thermally stratified accretion disk

NI98014-DAD **JA Sellwood and SA Balbus**
Differential rotation and turbulence in extended H I disks

NI98015-DAD **AM Fridman and OV Khoruzhii**
On nonlinear dynamics of 3D astrophysical disks

NI98016-DQC **RE Prange, R Narevich and O Zaitsev**
Quasiclassical surface of section perturbation theory

NI98017-DQC **A Sedrakyan**
Edge excitations of an incompressible fermionic liquid in a disorder magnetic field

NI98018-DAD **CF Gammie**
Accretion disk turbulence

NI98019-DAD **R Popham and CF Gammie**
Advection dominated accretion flows in the Kerr metric: II. Steady state global solutions

NI98020-DAD **CF Gammie and R Narayan**
What is the accretion rate in NGC 4258?

NI98021-DAD **CF Gammie**
Photon bubbles in accretion disks

NI98022-DAD **EC Ostriker, CF Gammie and JM Stone**
Kinetic and structural evolution of self-gravitating, magnetized clouds: 2.5-dimensional simulations of decaying turbulence

---